High-pressure evolution of silver iodate ($AgIO_3$) and the γ-$AgIO_3$ phase

Robin Turnbull [1,*] Josu Sánchez-Martín [1] Robert Oliva [2] Jordi Ibáñez [2] Catalin Popescu [3] Plácida Rodríguez-Hernández [4] Alfonso Muñoz [4] Gwilherm Nénert [5] David Vie [1] and Daniel Errandonea [1]

[1]*Departamento de Física Aplicada–Instituto de Ciencia de Materiales, MALTA Consolider, Team, Universidad de Valencia, Edificio de Investigación, C/Dr. Moliner 50, Burjassot, 46100 Valencia, Spain*

[2]*Geosciences Barcelona (GEO3BCN-CSIC), MALTA Consolider Team, C/Lluís Solé i Sabarís, s/n, 08028 Barcelona, Catalonia, Spain*

[3]*CELLS-ALBA Synchrotron Light Facility, 08290 Cerdanyola del Vallès, Barcelona, Spain*

[4]*Departamento de Física, Instituto de Materiales y Nanotecnología, MALTA Consolider Team, Universidad de La Laguna, La Laguna, E-38204 Tenerife, Spain*

[5]*4 Malvern Panalytical B. V., Almelo 7602 EA, The Netherlands*

(Received 21 June 2023; accepted 21 July 2023; published 25 August 2023)

A phase of silver iodate, γ-$AgIO_3$, has been obtained at ambient temperature by compressing α-$AgIO_3$ to 1.60(5) GPa. The γ-$AgIO_3$ crystal structure was identified via Rietveld refinement of high-pressure powder synchrotron x-ray diffraction. The γ-$AgIO_3$ reflections were indexed to an orthorhombic lattice (*Pbca*) with unit-cell dimensions of $a = 7.2945(12)$, $b = 15.0013(24)$, $c = 5.3904(9)$ Å, and $V = 589.85(29)$ Å^3 at 2.20(5) GPa. Density-functional theory calculations predict that γ-$AgIO_3$ is more stable than α-$AgIO_3$ above 0.15 GPa. The $\alpha \rightarrow \gamma$-phase transition is characterized by a decrease in the volume per formula unit of approximately 2% and it is reversible on decompression. Single-crystal optical-absorption measurements and density-functional theory calculations reveal the electronic band gap to decrease monotonically with increasing pressure in both α and γ phases, however the $\alpha \rightarrow \gamma$-phase transition (indirect $\rightarrow$ indirect) is characterized by an abrupt band-gap energy increase of approximately +0.18 eV. This pressure induced band-gap evolution is rationalized based on the I-O bond lengths. The γ phase may correspond to an intermediate step between the previously known α and β phases.

DOI: 10.1103/PhysRevMaterials.7.084606

I. INTRODUCTION

Metal iodate compounds exhibit a number of characteristics which make them desirable materials for applications as well as fundamental research [1]. Many metal iodate materials crystallize in noncentrosymmetric structures, resulting in nonlinear properties such as second harmonic generation [2], birefringence [3], photocatalysis [4], and piezoelectric response [5]. Regarding fundamental research, the most common building block of metal iodate materials, the IO_3 pyramid, possesses a lone electron pair (LEP) which results in halogen bonding [6] whereby the central iodine atom in the IO_3 unit additionally forms three weak I$\cdots$O bonds. The weak I$\cdots$O bonds are especially susceptible to the external control parameter of pressure, which can be used to control the interatomic distances and thereby tune emergent properties.

The α phase of silver iodate was structurally characterized in 1979 [7]. It is also the first metal iodate in which a pressure induced phase transition was observed [8]. In Ref. [8] the $\alpha \rightarrow \beta$-$AgIO_3$ transition was discovered in 2013 at pressure-temperature (*P-T*) conditions of 2.7 GPa and 260 °C. In the work of Ref. [7] the crystal structure of β-$AgIO_3$ was determined *ex situ* at ambient conditions. In the present work, we observe the new $\alpha \rightarrow \gamma$-$AgIO_3$ transition *in situ* at less extreme *P-T* conditions of 1.60(5) GPa and ambient temperature. Therefore, it is plausible that the *P-T* path followed in Ref. [7] in fact involved an intermediate state, the new γ-$AgIO_3$ phase, which went undetected in the compression sequence: $\alpha \rightarrow \gamma \rightarrow \beta$.

In the present work, the high-pressure evolution of $AgIO_3$ is investigated by powder synchrotron x-ray diffraction, single-crystal optical-absorption spectroscopy, and *ab initio* density-functional theory (DFT) calculations. A new phase of silver iodate, γ-$AgIO_3$, has been obtained at ambient temperature by compressing α-$AgIO_3$ to 1.60(5) GPa and the pressure evolution of the lattice parameters of the α and γ phases is investigated. Prior to the present work, the compressibility of $AgIO_3$ had not been studied. Furthermore, we present the first band-gap measurements and theoretical calculations of $AgIO_3$, finding the electronic band gap to decrease monotonically with increasing pressure in both α and γ phases. An abrupt increase of approximately +0.2 eV is found across the phase transition which is consistent with the decrease in the average length of the I-O bonds and in agreement with DFT calculations.

II. METHODS

A. Sample preparation

Monocrystalline α-$AgIO_3$ samples were prepared via a mixture of 0.5101 g of $AgNO_3$, 0.5304 g of HIO_3, and 10 mL of H_2O. The whitish mixture was introduced into a steel-jacketed Teflon hydrothermal reactor and heated at 220 °C for 72 h. Subsequently, it was cooled to room temperature at a rate of 10 °C/h. The resulting material was

*robin.turnbull@uv.es

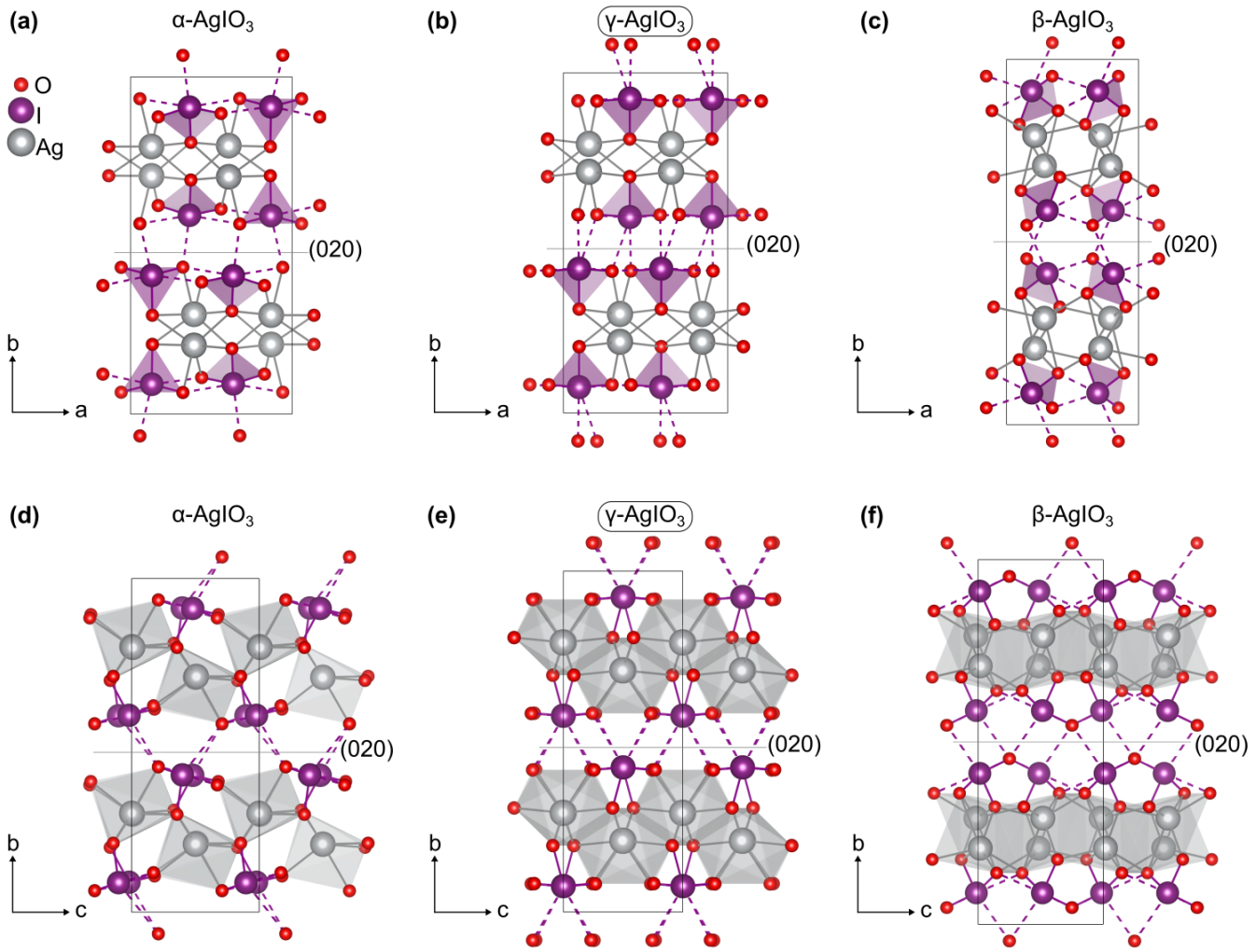

FIG. 1. Crystal structure of γ-$AgIO_3$ in comparison with α-$AgIO_3$ and β-$AgIO_3$. [(a)–(c)] α-, β-, and γ-$AgIO_3$ crystal structures projected along the crystallographic c axis. The IO_3 pyramid coordination polyhedron is shown in purple. [(d)–(f)] α-, β-, and γ-$AgIO_3$ crystal structures projected along the a axis. The AgO_6 coordination polyhedron is shown in grey. In all subpanels the (020) lattice plane is shown to highlight the layers of sheets parallel to the $(0k0)$ planes. Dashed lines represent I$\cdots$O halogen bonds where the bond length L fits the condition 2.0 Å $< L <$ 3.0 Å. The structure of α-$AgIO_3$ was reported in Ref. [8]. The structure of β-$AgIO_3$ was reported in Ref. [7]. The crystal structure images were rendered with VESTA [27].

filtered and washed with water, and finally dried in an oven at 60 °C.

Synthesis of polycrystalline α-$AgIO_3$ samples was carried out by the coprecipitation method. Separate aqueous solutions of $AgNO_3$ and NH_4IO_3 were prepared in beakers. After complete dissolution, solutions were mixed at ambient conditions. As soon as the solutions were mixed, a white precipitate appeared. This precipitate was washed several times with deionized water and recovered by centrifugation. To check for phase purity and to carry out Rietveld refinement of the obtained powder, the sample was loaded into a capillary of 0.3 mm diameter. X-ray powder diffraction was carried out using Mo $K_{\alpha 1,2}$ radiation in an Empyrean diffractometer equipped with a focusing mirror and a GaliPIX3D detector. Debye-Scherrer was necessary as preliminary characterization suggested strong preferred orientation. Rietveld refinement was carried out using the HIGHSCORE suite [9]. The obtained Rietveld fit of the starting material is shown in Supplemental Material Fig. 1 (Ref. [10]).

B. Measurements

Angle-dispersive powder XRD data were acquired on the BL04-MSPD beamline at ALBA Synchrotron [11] using a monochromatic beam of wavelength $\lambda = 0.4246$ Å focused to approximately 20 × 20 µm. The data were recorded on an SX165 Rayonix Mar charge-coupled device (CCD) detector. DIOPTAS [12] was used to integrate the 2D patterns which were then analyzed in POWDERCELL [13]. All powder diffraction measurements (P-XRD) were performed at room temperature. For HP measurements we used a membrane driven diamond anvil cell (DAC) from Almax-EasyLab, with an opening angle of 20° and anvil culets of 500 µm diameter. The gasket material was stainless steel with a sample chamber diameter of approximately 200 µm diameter and 70 µm depth. The pressure transmitting medium was a 4:1 methanol-ethanol mixture (ME) [14]. The polycrystalline α-$AgIO_3$ sample was ground under ME in a pestle and mortar for 10 min and then placed on the diamond anvil (diffraction side) with a small copper grain to be used as a pressure sensor [15].

Single-crystal absorption spectra were acquired in the ultraviolet/visible range on the in-house optical setup at the University of Valencia using a Maya spectrometer, an ultraviolet/visible lamp, fused silica lenses, and reflecting optical objectives. Single crystals of α-$AgIO_3$, approximately $70 \times 50 \times 15\,\mu m^3$ in size, were loaded into a membrane driven DACs with small ruby spheres for pressure determination [16]. The diamonds had culet sizes of approximately 400 μm. The gasket material was stainless steel with a sample chamber diameter of approximately 250 μm diameter and 50 μm depth. 16:3:1 methanol-ethanol-water was used as pressure transmitting medium (PTM) as it has the same hydrostatic pressure range as the 4:1 ME mixture used in XRD experiments [14]. The light transmitted through the PTM was used as the reference $[I_0(\omega)]$ to normalize the light transmitted through the sample $[I(\omega)]$.

C. *Ab initio* density functional theory calculations

In this work simulations were performed with the well-known plane wave pseudopotential method in the framework of the density-functional theory [17] implemented in the Vienna Ab initio Simulation Package, VASP [18,19]. We used the projector augmented wave (PAW) pseudopotentials [20,21] provided in the VASP pseudopotentials database; the exchange-correlation term was described using the generalized gradient approximation (GGA), using the AM05 [22,23] functional. Brillouin zone k-point sampling was performed using a dense Monkhorst-Pack [24] sampling of $4 \times 2 \times 4$, and $4 \times 2 \times 6$ for the α- and γ-$AgIO_3$ structures. A plane-wave basis set with an energy cutoff of 540 eV was used to ensure accurate and highly converged results. For the different analyzed structures, all degrees of freedom, lattice parameters, and internal atomic parameters were fully relaxed with self-consistent convergence criteria of $0.003\,eV/Å$ for the atomic forces, total energy of 10^{-6} eV, and the diagonal terms of the stress tensor below 0.1 GPa. From our simulations we obtain a set of volume, energy, and pressure data that we fit using a Birch-Murnaghan [25] equation of state.

The electronic band structures of the α- and γ-$AgIO_3$ structures at different pressures along high-symmetry directions [26] were obtained for the relaxed structures at different pressures. This procedure allows us to obtain the band gap, its evolution with pressure, and the projected density of states.

III. RESULTS AND DISCUSSION

A. γ-$AgIO_3$ crystal structure

The structure of α-$AgIO_3$ is reported in detail elsewhere [6,7] and described briefly here to facilitate comparison with the γ-$AgIO_3$ structure. In the present work, Rietveld refinement of powder XRD data confirm the α-$AgIO_3$ structure at ambient conditions, finding an orthorhombic lattice ($Pbc2_1$) with unit-cell dimensions of $a = 7.265(4)$, $b = 15.170(8)$, $c = 5.786(3)$Å, and $V = 637(1)\,Å^3$. As shown in Figs. 1(a) and 1(d), the α-$AgIO_3$ crystal structure consists of layers of sheets parallel to the (010) plane. The essential building blocks of the α-$AgIO_3$ structure are the IO_3 unit, which exhibits three short I-O bonds [ranging 1.787(10)–1.854(10) Å] oriented away from the I lone electron pair, forming the typical IO_3 pyramid, in addition to three long I···O halogen bonds [ranging 2.692(13)–2.985(12) Å]. Each IO_3 unit exhibits two I···O halogen bonds oriented in plane with the layers, and a third I···O bond interconnecting the sheets of layers. Since there are two crystallographically unique I atoms, there are two I···O halogen bonds interconnecting the layers: $l(I2\cdots O2) = 2.692(13)$ Å and $l(I1\cdots O4) = 2.985(12)$ Å, shown as dashed lines in Fig. 1. However, there is only one layer-interconnecting I···O bond per I atom. The Ag atoms are six-coordinated by O atoms, forming distorted triangular prisms which are roughly oriented along the [001] direction.

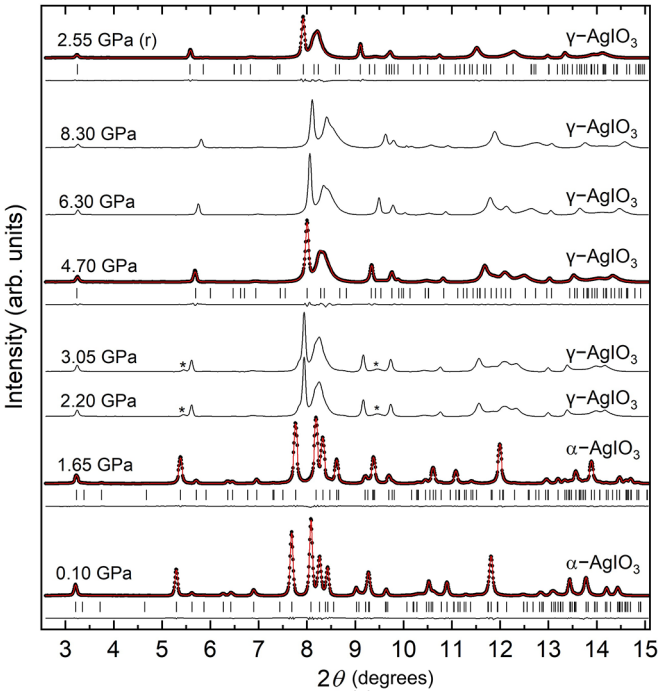

FIG. 2. Integrated high-pressure synchrotron powder x-ray diffraction patterns from α- and γ-$AgIO_3$. Rietveld profiles are shown in red. The observed XRD data are shown via black symbols and the residual is shown underneath via black lines. When profiles (red) are not shown the raw data are shown via black lines. Bragg reflection positions are shown via vertical tick marks below the patterns. The pressure of each diffraction pattern is indicated in the figure (±0.05 GPa) as well as the $AgIO_3$ phase (α or γ) to which the patterns correspond. Asterisks (∗) mark reflections from α-$AgIO_3$ which are still observable after the onset of the α- to γ-$AgIO_3$ phase transition.

The structure of γ-$AgIO_3$ is closely related to that of α-$AgIO_3$ and it is shown in Figs. 1(b) and 1(e). From Rietveld refinement of the high-pressure powder XRD data, the γ-$AgIO_3$ reflections were indexed to an orthorhombic lattice ($Pbca$) with unit-cell dimensions of $a = 7.2945(12)$, $b = 15.0013(24)$, $c = 5.3904(9)$ Å, and $V = 589.85(29)\,Å^3$ at 2.2 GPa (Fig. 2). The atomic coordinates of γ-$AgIO_3$ are reported in Supplemental Material Table 1 [10]. The γ-$AgIO_3$ crystal structure also consists of layers of sheets parallel to the (010) plane. One of the principal differences between the α-$AgIO_3$ and γ-$AgIO_3$ structures is that in γ-$AgIO_3$ each I atom contributes two I···O layer-interconnecting halogen

TABLE I. Basic crystal data for α- and γ-$AgIO_3$ based on powder XRD data and DFT calculations.

Phase	α-$AgIO_3$		γ-$AgIO_3$	
Data	Experiment	DFT	Experiment	DFT
Pressure (GPa)	0.0 (ambient)	0.0	2.20(5)	2.0
Crystal system	orthorhombic	orthorhombic	orthorhombic	orthorhombic
Space group	$Pbc2_1$	$Pbc2_1$	$Pbca$	$Pbca$
a(Å)	7.265(1)	7.11155	7.2945(12)	7.23336
b(Å)	15.170(4)	15.20303	15.0013(24)	14.94622
c(Å)	5.786(1)	5.78077	5.3904(9)	5.38183
V(Å^3)	637.67(26)	625.0	589.85(29)	581.83777
Z	6	6	6	6

bonds. In contrast, in α-$AgIO_3$ there is only one layer-interconnecting I$\cdots$O bond per I atom. In γ-$AgIO_3$ there is only one crystallographically unique I atom. Therefore, the lengths l of the two interconnecting I$\cdots$O halogen bonds per I atom are $l(\text{I}\cdots\text{O1}) = 2.843(20)$ Å and $l(\text{I}\cdots\text{O2}) = 2.646(20)$ Å. Another noteworthy difference between the α and γ structures is that in γ-$AgIO_3$ the I atoms exhibit an additional I$\cdots$O halogen bond, making a total of four rather than three bonds, ranging 2.522(20)–2.843(20) Å. As in α-$AgIO_3$, the Ag atoms in γ-$AgIO_3$ are six-coordinated by O atoms but with a heavily distorted octahedral geometry. In both α-$AgIO_3$ and γ-$AgIO_3$ one layer is mapped onto the next layer in the sequence by a 2_1 screw axis along the b axis and a reflection in the ac plane. Basic experimental and DFT calculation crystal data for α- and γ-$AgIO_3$ are given in Table I.

Although the structure of β-$AgIO_3$ has not been measured in this work, it is worthy of mention since γ-$AgIO_3$ could be a previously unobserved phase in the compression sequence: $\alpha \rightarrow \gamma \rightarrow \beta$. According to Ref. [8], β-$AgIO_3$ is, like the α and γ phases, characterized by an orthorhombic lattice (in this case in the space group $Pbca$) with the following lattice parameters at ambient pressure: $a = 6.137(2)$ Å, $b = 16.980(4)$ Å, $c = 5.827(1)$ Å and $V = 607.3(3)$ Å^3. In Fig. 1 the unit cell of β-$AgIO_3$ has been translated by $0.25b$ to aid comparison with the other phases. In β-$AgIO_3$ there is only one I$\cdots$O interaction between the layers, $l(\text{I1}\cdots\text{O2}) = 2.870$ Å, thereby making γ-$AgIO_3$ unique since it is the only $AgIO_3$ phase to exhibit two interconnecting halogen bonds per I atom. In β-$AgIO_3$ the Ag atoms are, as in all three phases, six-coordinated by oxygen atoms. As in α-$AgIO_3$, the AgO_6 coordination polyhedra in β-$AgIO_3$ have a slightly distorted triangular prism configuration, making the distorted AgO_6 octahedra of γ-$AgIO_3$ another unique difference.

B. Pressure-induced structural evolution of $AgIO_3$ and compressibility

The $\alpha \rightarrow \beta$-$AgIO_3$ transition is not reversible on decompression and β-$AgIO_3$ is recoverable to ambient conditions [8]. In contrast, the $\alpha \rightarrow \gamma$-$AgIO_3$ transition of the present work is reversible on decompression and α-$AgIO_3$ is recovered at ambient conditions. According to the results of DFT calculations shown in Fig. 3, the most thermodynamically stable phase at ambient conditions is the α phase, therefore the metastability of the β-$AgIO_3$ can be explained by a kinetic barrier. This is consistent with the fact that the forward $\alpha \rightarrow \beta$-$AgIO_3$ transition requires high temperatures (at least a pressure below 2 GPa) suggesting a kinetically hindered transition. Looking at the bottom row of Fig. 1, it is clear that the $\alpha \rightarrow \beta$-$AgIO_3$ transition is reconstructive since there is significant rearrangement of the IO_3 units in the β-$AgIO_3$ structure. In the β-$AgIO_3$ structure the IO_3 units are aligned opposite each other between different layers. In contrast, the $\alpha \rightarrow \gamma$-$AgIO_3$ transition appears to be a displacive phase transition, since there is no significant rearrangement of atomic positions, and the transition is reversible on decompression. The critical pressure between the α and γ phases according to the enthalpy calculations in Fig. 3 (0.15 GPa) does not account for kinetic effects and is therefore an underestimation of the experimental value [1.60(5) GPa]. Assuming that the ambient temperature compression sequence $\alpha \rightarrow \gamma \rightarrow \beta$ reinforced by the DFT calculation results is correct, then, as shown in Fig. 1, the AgO_6 units gradually compact together on compression, thereby making a sublayer of edge sharing AgO_6 units. This compression of the edge sharing AgO_6 units expels the IO_3 units into the immediate interlayer area. It is plausible that on further compression above 8 GPa

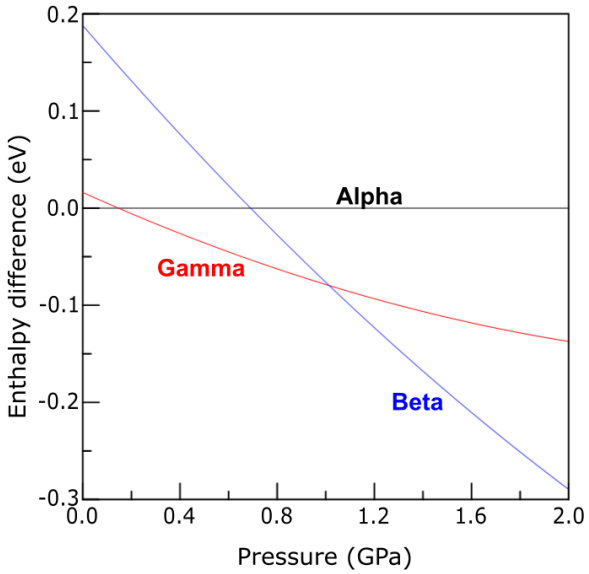

FIG. 3. Calculated enthalpy difference for γ-$AgIO_3$ (red) and β-$AgIO_3$ (blue) relative to α-$AgIO_3$ (black).

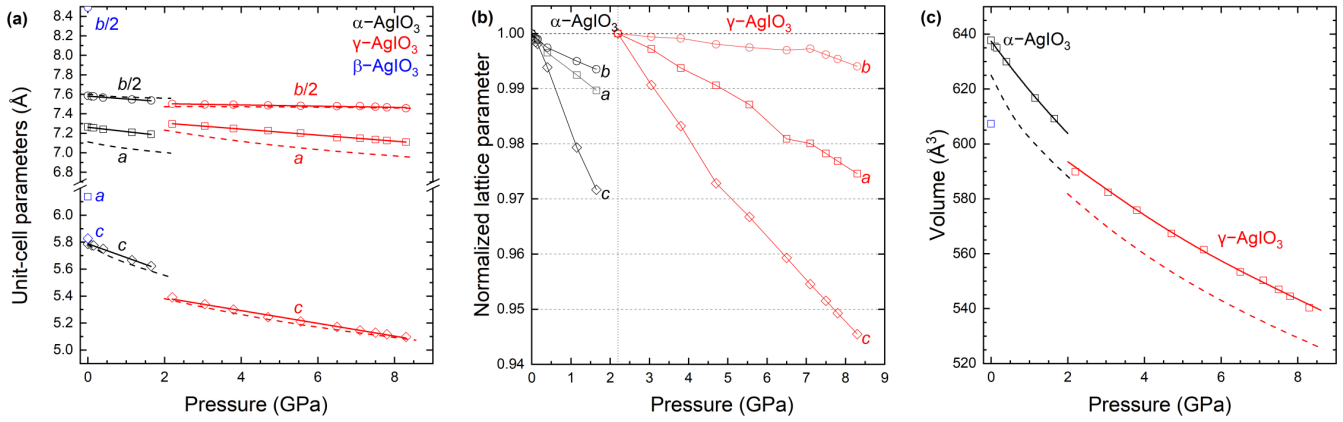

FIG. 4. Pressure-induced evolution of $AgIO_3$ unit-cell parameters and volume. (a) Unit-cell parameters a, b, and c. (b) Normalized unit-cell parameters. (c) Unit-cell volume. As in Fig. 3, all data for γ-$AgIO_3$ are shown in red, α-$AgIO_3$ in black, and β-$AgIO_3$ in blue. Experimental data are shown with symbols. The corresponding fitted equations of state are shown with solid lines. Equations of state determined by density functional calculations are shown with dashed lines.

γ-$AgIO_3$ would transition to the lower enthalpy β-$AgIO_3$ structure at ambient temperature. This would be an interesting and easily achievable direction for future works. As discussed later in Sec. III C, it is possible that in the present work the $\gamma \rightarrow \beta-AgIO_3$ transition has been observed in monocrystalline absorption measurements above 15 GPa, however XRD measurements would be necessary to unambiguously clarify this hypothesis.

The crystal lattice parameters, as determined from the high-pressure powder crystal XRD experiments, are plotted in Fig. 4(a). The normalized crystal lattice parameters are plotted in Fig. 4(b). The corresponding unit-cell volume is plotted as a function of pressure in Fig. 4(c). The compressibilities of the $AgIO_3$ phases have not previously been studied. The experimental volume data [Fig. 4(c)] for both the α- and γ-$AgIO_3$ phases have been fitted with second order Birch-Murnaghan (BM) [17,28] equations of state (EoS) using the EosFit7–GUI [29], resulting in converged parameters for α-$AgIO_3$ of $V_0 = 637.6(2)$ Å^3, $B_0 = 32.8(4)$ GPa, $B_0^{'} = 4$ (fixed), and for γ-$AgIO_3$ of $V_0 = 614.8(9)$ Å^3, $B_0 = 50.4(9)$GPa, $B_0^{'} = 4$ (fixed). The bulk moduli B_0 determined from DFT are in excellent agreement with the following values for α- and γ-$AgIO_3$ respectively: 30(3) and 46(1) GPa, with zero pressure volumes, V_0, of 623(2) and 604(1) Å^3 respectively. The slight underestimation of the zero-pressure volume is a common result of the DFT approach used in our calculations. Although the compressibility of β-$AgIO_3$ has not been measured in this (or any previous) work, the data obtained here nonetheless infer a minimum value on the expected bulk modulus of $B_{0,\beta} \geqslant B_{0,\gamma} = 50.4(9)$ GPa. The abrupt decrease in unit volume across the $\alpha \rightarrow \gamma$ transition is approximately 2%, thereby identifying the transition as first order. The γ-$AgIO_3$ phase remained the only phase in the XRD patterns until the maximum pressure studied of 8.30(5) GPa. Upon sample decompression the transition was found to be reversible.

Interestingly, the normalized lattice parameters [see Fig. 4(b)] show that despite being the shortest, the c axis is the most compressible. The decrease of the length of the c axis is probably achieved by reduced tilting of the AgO_6 polyhedra. Additionally, Ag-O bonds [30] are much more compressible than similar bonds, for example: Zn-O, Co-O, Ca-O, Fe-O, etc. This is observed by the fact that oxides like ZnO, CaO, FeO, etc., have bulk moduli higher than 100 GPa, while Ag_2O has a bulk modulus of 74 GP (Ref. [31]). The reduced tilting of the AgO_6 polyhedra also explains the increase observed in the lattice parameter a across the phase transition since the reduced tilting causes a slight increase in layer thickness.

C. Electronic structure

The pressure evolution of the $AgIO_3$ band gap was determined by single crystal UV-vis transmission spectroscopy and DFT calculations. (See the Measurements section above for more details.) At ambient pressure the band gap was measured at 3.80(5) eV (2.21 eV) in experiment (DFT calculations). This energy measured experimentally corresponds to the ultraviolet region of the electromagnetic spectrum, which is consistent with the colorless crystal shown in the inset in Fig. 4(c). As shown in Fig. 5, the experimentally measured band-gap energy of the initial α-$AgIO_3$ phase decreases monotonically with pressure to 3.74(4) eV at 1.36(5) GPa. The band gap then opens again due to the $\alpha \rightarrow \gamma$-$AgIO_3$ phase transition, where it abruptly increases by +0.18 eV to 3.92 eV between 1.66(5) and 1.80(5) GPa. With increasing pressure, the band-gap energy of the γ phase also decreases monotonically until the maximum pressure studied in this work [20.2(5) GPa]. As expected, the band-gap energy according to DFT calculations is underestimated relative to the experimental results. In contrast, the eV/GPa gradient in both phases and the jump across the transition are similar to experiment. Therefore, in order to facilitate a better comparison between experiment and theory, the band-gap energies according to the DFT results have been upshifted by 1.65 GPa in Fig. 5. Typically, DFT calculations will underestimate the band gap due to the approximations used in the GGA-PBEsol description [32]. Band structure calculations [Figs. 6(a) and 6(b)] reveal the band gap to be indirect in both α and γ phases. The $\alpha \rightarrow \gamma$-$AgIO_3$ transition pressure observed in these monocrystalline absorption measurements

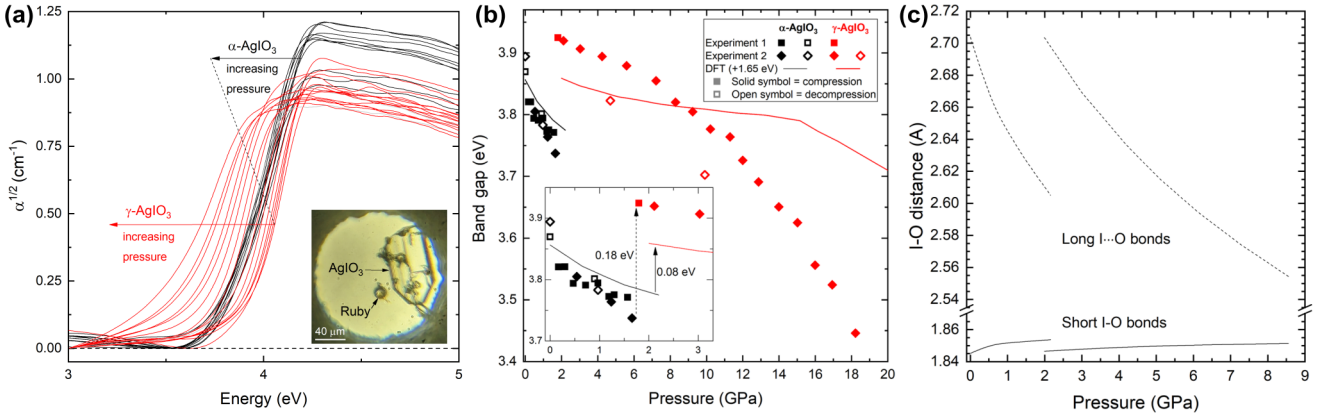

FIG. 5. α- and γ-$AgIO_3$ band gap and I-O bond evolution with pressure according to experiment and DFT calculations. (a) High pressure absorbance spectra of α- and γ-$AgIO_3$. The corresponding band-gap energies are shown in Fig. 5(b). (b) Experimentally measured and calculated band gap of $AgIO_3$ up to 18 GPa. Experimental data are shown with symbols. DFT calculation results are shown with solid lines. (c) The interatomic distances were calculated using DFT. The short I-O distance is shown with solid lines. The longer I $\cdots$ O distance is shown with dashed lines.

[1.66(5) GPa] agrees with that observed in the polycrystalline XRD measurements [between 1.65(5) and 2.20(5) GPa].

The pressure-induced evolution of the $AgIO_3$ band gap can be explained by the changes in the I-O bond lengths. As discussed in Sec. III A, the IO_3 unit in $AgIO_3$ exhibits three short I-O bonds where the bond length, $L < 2$ Å, and three (or four in the case of γ) long I $\cdots$ O halogen bonds where the bond length L fits the condition 2.0 Å $< L <$ 3.0 Å. The I-O and I $\cdots$ O bond distances in $AgIO_3$ as a function of pressure as calculated by DFT are shown in Fig. 5(c). In a previous work, Ref. [33], it is explained in detail how the band-gap energy in iodates is inversely proportional to the average

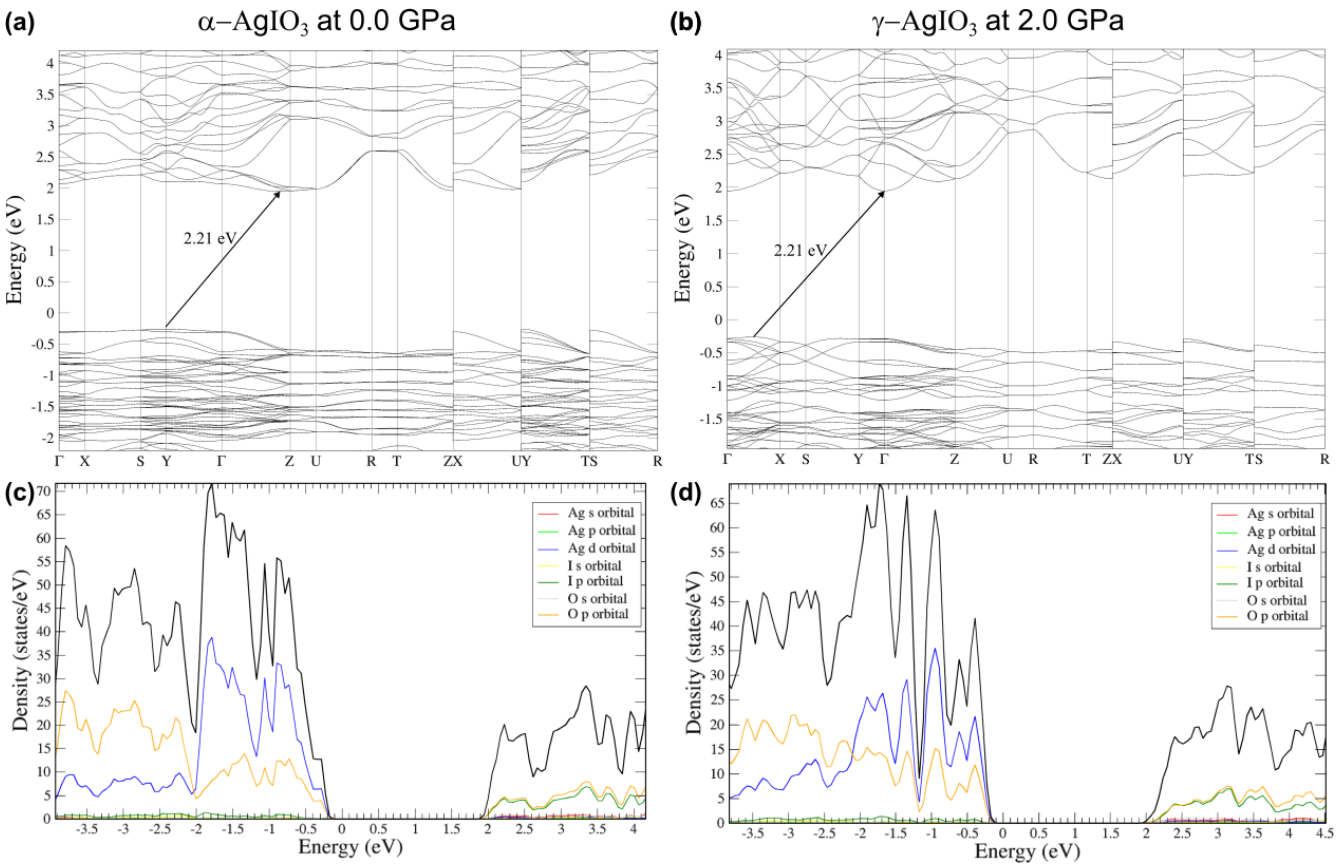

FIG. 6. The band structures of α- and γ-$AgIO_3$ at 0.0 and 2.0 GPa respectively. The indirect nature of both α and γ band-gap energies is indicated by arrows.

I-O bond length, i.e., as the I-O bond length increases, the band-gap energy decreases. Therefore, there is an excellent agreement between the experimentally determined band gap and the calculated I-O bond lengths. In both the α and γ phases, the I-O bond length increases with pressure, resulting in a lowering of the band gap. Additionally, across the $\alpha \rightarrow \gamma$-phase transition the average I-O bond length decreases, causing a jump in the band-gap energy to approximately its initial ambient pressure value. In Fig. 5(b) it is noteworthy that the decrease in length of the long I···O bonds causes the increase in length of the short I-O bonds. Also, it should be mentioned that influence of the long I···O bonds on the overall band gap is much smaller than that of the shorter I-O bonds due to the larger distance between the I and O atoms. According to the DFT calculations shown in Figs. 6(c) and 6(d), the main contributions to the conduction band in α- and γ-$AgIO_3$ are the I and O orbitals (green and orange respectively), which is consistent with the general observation that the optical/electrical properties of iodates, and $AgIO_3$ in particular, depend on the I-O bond length. Regarding the topology of the band structures, the dispersion in both α and γ phases appears to be similar, suggesting that the orbital overlap between Op and Ip states of different IO_3 units remains similar in both phases, which is consistent with the nonreconstructive phase transition.

IV. CONCLUSIONS

In this work the high-pressure evolution of $AgIO_3$ was investigated by powder synchrotron x-ray diffraction, single crystal optical absorption spectroscopy and *ab initio* density functional theory calculations. A different phase of silver iodate, γ-$AgIO_3$, was obtained at ambient temperature by compression of α-$AgIO_3$ to 1.60(5) GPa. The γ-$AgIO_3$ crystal structure was identified via Rietveld refinement of high-pressure powder synchrotron x-ray diffraction, finding an orthorhombic lattice (*Pbca*) with unit-cell dimensions of $a = 7.2945(12)$, $b = 15.0013(24)$, $c = 5.3904(9)$ Å and $V = 589.85(29)$ Å^3 at 2.20(5) GPa. The γ-$AgIO_3$ phase may represent an intermediate step between the previously known α and β phases. The present work represents an investigation into the pressure-induced structural evolution and compressibility of $AgIO_3$, reporting changes in crystal lattice parameters and I-O bond lengths. The α and γ phases are found to have bulk moduli B_0 of 32.8(4) and 50.4(9) GPa respectively, thereby putting a lower limit on the expected bulk modulus of the β phase. The $\alpha \rightarrow \gamma$ phase transition, which is reversible on decompression, was found to be characterized by a decrease in the volume per formula unit of approximately 2% thereby identifying it as a first order transition. Density functional theory calculations found γ-$AgIO_3$ to be more stable than α-$AgIO_3$ above 0.15 GPa. Furthermore, this work also presents band-gap measurements and calculations of $AgIO_3$, finding the electronic band gap to decrease monotonically with increasing pressure in both α and γ phases, accompanied by an abrupt increase of approximately +0.2 eV across the indirect → indirect band-gap phase transition. This work makes clear arguments for future work towards the high-pressure characterization of the β-$AgIO_3$ phase which is currently missing in the literature.

All relevant data are available from the corresponding author upon reasonable request.

ACKNOWLEDGMENTS

The authors acknowledge financial support from the Spanish Research Agency (AEI) and Spanish Ministry of Science and Investigation (MCIN) under Projects No. PID 2019106383GB-C41/C43 (DOI: 10.13039/501100011033) and No. PID2022-138076NB-C41, and Projects No. PGC2018-101464-B-I00 and No. PGC2018-097520-A-I00 (cofinanced by EU FEDER funds). The authors acknowledge financial support from the MALTA Consolider Team network, under Projects No. RED2018-102612-T and No. RED2022-134388-T. R.T. acknowledges funding from the Generalitat Valenciana for Postdoctoral Fellowship No. CIAPOS/2021/20. J.S.-M. acknowledges the Spanish Ministry of Science, Innovation and Universities for the PRE2020-092198 fellowship. This study forms part of the Advanced Materials program and is supported by MCIN with funding from European Union Next Generation EU (PRTR-C17.I1) and by the Generalitat Valenciana (Grant No. MFA/2022/007). D.E. acknowledges the financial support from the Generalitat Valenciana under Grant No. PROMETEO CIPROM/2021/075-GREENMAT. C.P. acknowledges the financial support from Spanish Ministry of Science and Investigation through Project No. PID2021-125927NB-C21. The authors also thank ALBA synchrotron light source for a funded experiment under Proposal No. 2021085271 at the MSPD-BL04 beamline.

[1] A. Liang, R. Turnbull, and D. Errandonea, A review on the advancements in the characterization of the high-pressure properties of iodates, Prog. Mater. Sci. **136**, 101092 (2023).

[2] F. F. Mao, C. L. Hu, X. Xu, D. Yan, B. P. Yang, and J. G. Mao, $Bi(IO_3)F_2$: The first metal iodate fluoride with a very strong second harmonic generation effect, Angew. Chem. **129**, 2183 (2017).

[3] M. Gai, T. Tong, Y. Wang, Z. Yang, and S. Pan, New alkaline-earth metal fluoroiodates exhibiting large birefringence and short ultraviolet cutoff edge with highly polarizable $(IO_3F)^{2-}$ Units, Chem. Mater. **32**, 5723 (2020).

[4] H. Huang, Y. He, Y. Guo, R. He, Z. Lin, and Y. Zhang, Hydrothermal synthesis, nonlinear optical property and photocatalytic activity of a non-centrosymmetric $AgIO_3$ photocatalyst under UV and visible light irradiation, Solid State Sci. **46**, 37 (2015).

[5] J. Zhang, X. Du, S. H. Ke, B. Xu, G. Zheng, D. A. Rowlands, and K. Yao, Dielectric, piezoelectric and nonlinear optical properties of polar iodate $BiO(IO_3)$ from first-principles studies, J. Solid State Chem. **281**, 121057 (2020).

[6] Y. V. Nelyubina, M. Y. Antipin, and K. A. Lyssenko, Extremely short halogen bond: The nature and energy of iodine-oxygen

interactions in crystalline iodic acid, Mendeleev Commun. **21**, 250 (2011).

[7] Y. Suffren, I. Gautier-Luneau, C. Darie, C. Goujon, M. Legendre, and O. Leynaud, First evidence of a phase transition in a high-pressure metal iodate: Structural and thermal studies of $AgIO_3$ polymorphs, Eur. J. Inorg. Chem. **20**, 3526 (2013).

[8] R. Masse and J. C. Guitel, Préparation chimique et structure cristalline de l'iodate d'argent $AgIO_3$, J. Solid State Chem. **32**, 177 (1980).

[9] T. Degen, M. Sadki, E. Bron, U. König, and G. Nénert, The highscore suite, Powder Diffr. **29**, S13 (2014).

[10] See Supplemental Material at http://link.aps.org/supplemental/10.1103/PhysRevMaterials.7.084606 for the obtained Rietveld fit of the starting material (Supplemental Fig. 1) and the atomic coordinates of the high-pressure phase γ-$AgIO_3$ (Supplemental Table 1).

[11] F. Fauth, I. Peral, C. Popescu, and M. Knapp, The new material science powder diffraction beamline at ALBA synchrotron, Powder Diffr. **28**, S360 (2013).

[12] C. Prescher and V. Prakapenka, DIOPTAS: A program for reduction of two-dimensional x-ray diffraction data and data exploration, High Press. Res. **35**, 223 (2015).

[13] W. Kraus and G. Nolze, POWDER CELL-a program for the representation and manipulation of crystal structures and calculation of the resulting x-ray powder patterns, J. Appl. Crystallogr. **29**, 301 (1996).

[14] S. Klotz, J. C. Chervin, P. Munsch, and G. Le Marchand, Hydrostatic limits of 11 pressure transmitting media, J. Phys. D **42**, 075413 (2009).

[15] A. Dewaele, P. Loubeyre, and M. Mezouar, Equations of state of six metals above 94 GPa, Phys. Rev. B **70**, 094112 (2004).

[16] G. Shen, Y. Wang, A. Dewaele, C. Wu, D. E. Fratanduono, J. Eggert, S. Klotz, K. F. Dziubek, P. Loubeyre, O. V. Fat'yanov, and P. D. Asimow, Toward an international practical pressure scale: A proposal for an IPPS ruby gauge (IPPS-Ruby2020), High Press. Res. **40**, 299 (2020).

[17] P. Hohenberg and W. Kohn, Inhomogeneous electron gas, Phys. Rev. **136**, B864 (1964).

[18] G. Kresse and J. Furthmüller, Efficiency of *ab-initio* total energy calculations for metals and semiconductors using a plane-wave basis set, Comput. Mater. Sci. **6**, 15 (1996).

[19] G. Kresse and J. Furthmüller, Efficient iterative schemes for *ab initio* total-energy calculations using a plane-wave basis set, Phys. Rev. B **54**, 11169 (1996).

[20] P. E. Blöchl, Projector augmented-wave method, Phys. Rev. B **50**, 17953 (1994).

[21] G. Kresse and D. Joubert, From ultrasoft pseudopotentials to the projector augmented-wave method, Phys. Rev. B **59**, 1758 (1999).

[22] R. Armiento and A. E. Mattsson, Functional designed to include surface effects in selfconsistent density functional theory, Phys. Rev. B **72**, 085108 (2005).

[23] A. E. Mattsson, R. Armiento, J. Paier, G. Kresse, J. M. Wills, and T. R. Mattsson, The AM05 density functional applied to solids, J. Chem. Phys. **128**, 084714 (2008).

[24] H. J. Monkhorst and J. D. Pack, Special points for Brillouin-zone integrations, Phys. Rev. B **13**, 5188 (1976).

[25] F. Birch, Finite elastic strain of cubic crystals, Phys. Rev. **71**, 809 (1947).

[26] Y. Hinuma, G. Pizzi, Y. Kumagai, F. Oba, and I. Tanaka, Band structure diagram paths based on crystallography, Comput. Mater. Sci. **128**, 140 (2017).

[27] K. Momma and F. Izumi, *VESTA*: A three-dimensional visualization system for electronic and structural analysis, J. Appl. Crystallogr. **41**, 653 (2008).

[28] R. J. Angel, Equations of state, Rev. Mineral. Geochem. **41**, 35 (2000).

[29] J. Gonzalez-Platas, M. Alvaro, F. Nestola, and R. Angel, EosFit7-GUI: A new graphical user interface for equation of state calculations, analyses and teaching, J. Appl. Crystallogr. **49**, 1377 (2016).

[30] A. Deb and A. K. Chatterjee, The electronic structure and chemical bonding mechanism of silver oxide, J. Phys.: Condens. Matter **10**, 11719 (1998).

[31] F. Pei, S. Wu, G. Wang, M. Xu, S. Y. Wang, L. Chen, and Y. Jia, Electronic and optical properties of noble metal oxides M_2O (M = Cu, Ag, and Au): First-principles study, J. Kor. Phys. Soc. **55**, 1243 (2009).

[32] M. K. Y. Chan and G. Ceder, Efficient Band Gap Prediction for Solids, Phys. Rev. Lett. **105**, 196403 (2010).

[33] A. Liang, R. Turnbull, P. Rodriguez-Hernandez, A. Muñoz, M. Jasmine, L. T. Shi, and D. Errandonea, General relationship between the band-gap energy and iodine-oxygen bond distance in metal iodates, Phys. Rev. Mater. **6**, 044603 (2022).